Volume 214, Number 2, June 2022

Journal of Structural Biology

ELSEVIER

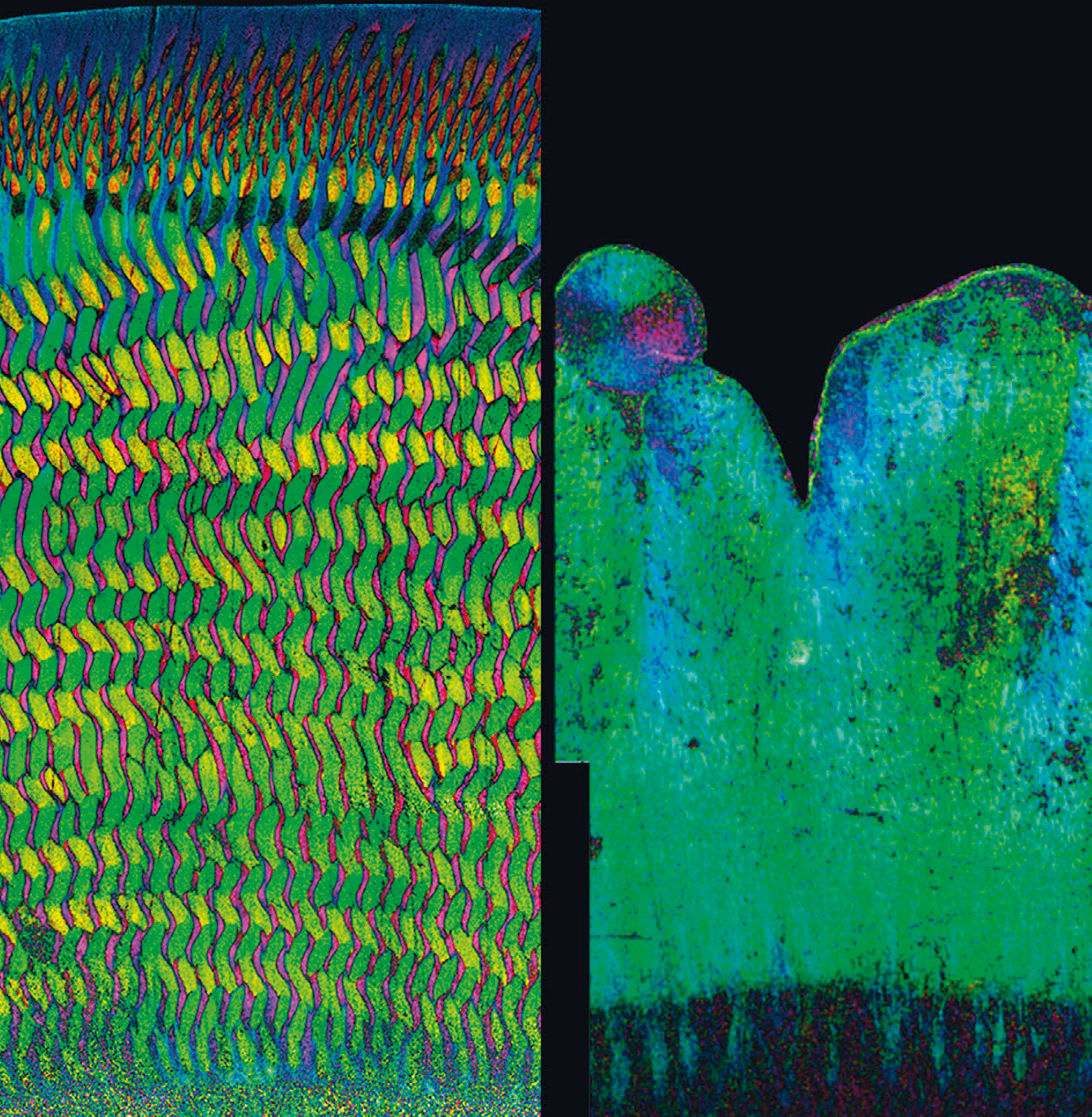

Journal of Structural Biology 214 (2022) 107844

Contents lists available at ScienceDirect

Journal of Structural Biology

journal homepage: www.elsevier.com/locate/yjsbi

Research Article

Loss of biological control of enamel mineralization in amelogenin-phosphorylation-deficient mice

Cayla A. Stifler[a], Hajime Yamazaki[b,1], Pupa U.P.A. Gilbert[a,c,d,2], Henry C. Margolis[b,e,2], Elia Beniash[b,f,*]

[a] Dept. of Physics, University of Wisconsin Madison, WI, USA
[b] Department of Oral and Craniofacial Sciences, Center for Craniofacial Regeneration, School of Dental Medicine, University of Pittsburgh, PA, USA
[c] Departments of Chemistry, Materials Science and Engineering, Geoscience, University of Wisconsin Madison, WI, USA
[d] Lawrence Berkeley National Laboratory, Chemical Sciences Division, Berkeley, CA, USA
[e] Department of Periodontics and Preventive Dentistry, School of Dental Medicine, University of Pittsburgh, PA, USA
[f] Department of Bioengineering, Swanson School of Engineering, University of Pittsburgh, PA, USA

ARTICLE INFO

Keywords:
Dental enamel
Amelogenin
Biomineralization
Phosphorylation

ABSTRACT

Amelogenin, the most abundant enamel matrix protein, plays several critical roles in enamel formation. Importantly, we previously found that the singular phosphorylation site at Ser16 in amelogenin plays an essential role in amelogenesis. Studies of genetically knock-in (KI) modified mice in which Ser16 in amelogenin is substituted with Ala that prevents amelogenin phosphorylation, and *in vitro* mineralization experiments, have shown that phosphorylated amelogenin transiently stabilizes amorphous calcium phosphate (ACP), the initial mineral phase in forming enamel. Furthermore, KI mice exhibit dramatic differences in the enamel structure compared with wild type (WT) mice, including thinner enamel lacking enamel rods and ectopic surface calcifications. Here, we now demonstrate that amelogenin phosphorylation also affects the organization and composition of mature enamel mineral. We compared WT, KI, and heterozygous (HET) enamel and found that in the WT elongated crystals are co-oriented within each rod, however, their *c*-axes are not aligned with the rods' axes. In contrast, in rod-less KI enamel, crystalline *c*-axes are less co-oriented, with misorientation progressively increasing toward the enamel surface, which contains spherulites, with a morphology consistent with abiotic formation. Furthermore, we found significant differences in enamel hardness and carbonate content between the genotypes. ACP was also observed in the interrod of WT and HET enamel, and throughout aprismatic KI enamel. In conclusion, amelogenin phosphorylation plays crucial roles in controlling structural, crystallographic, mechanical, and compositional characteristics of dental enamel. Thus, loss of amelogenin phosphorylation leads to a reduction in the biological control over the enamel mineralization process.

1. Introduction

Dental enamel is the most mineralized tissue in the human body, comprising roughly 96% apatitic mineral by weight. It is a highly resilient tissue with a unique combination of extraordinary hardness and fracture toughness (Bajaj and Arola, 2009; Chai et al., 2009), and can be considered a pinnacle of biomineral evolution. Even though mature enamel is an acellular tissue, and cannot, therefore, be remodeled and repaired like bone, it can last a lifetime through millions of cycles of mastication without catastrophic failure in the often harsh chemical environment of the oral cavity (*e.g.* acidic foods and beverages). The secret to this unique resilience of enamel is in its sophisticated structural organization (Beniash et al., 2019; Wilmers and Bargmann, 2020; Yilmaz et al., 2015) and its graded chemical composition (Weatherell et al., 1974; Xu et al., 2012). The basic building block of mammalian enamel is the enamel rod – an array of extremely long apatitic crystallites. Groups of enamel rods form complex interwoven arrangements, known as the enamel decussating pattern. Such patterns are species, tooth type and

---

[*] Corresponding author at: Department of Oral and Craniofacial Sciences, Center for Craniofacial Regeneration, School of Dental Medicine, University of Pittsburgh, PA, USA.

E-mail address: ebeniash@pitt.edu (E. Beniash).

[1] No longer with the University of Pittsburgh.

[2] Previously publishing as Gelsomina De Stasio.

https://doi.org/10.1016/j.jsb.2022.107844
Received 17 December 2021; Received in revised form 18 February 2022; Accepted 22 February 2022

tooth surface specific, and are optimally adapted to their function (Maas and Dumont, 1999).

Enamel is secreted by specialized epithelial cells – ameloblasts, equipped with a sophisticated secretory apparatus called the Tomes' process. Each enamel rod is formed by one Tomes' process, and enamel decussation is achieved by highly coordinated movement of groups of ameloblasts (Cox, 2013; Nishikawa, 2017). Enamel starts as a self-assembled protein gel holding together a template of nascent mineral crystallites. This initial secretory enamel comprises, in roughly equal amounts, mineral, organics and water. Although secretory enamel is much less mineralized, the complex architecture of the mature tissue is determined at this initial stage of development. During enamel maturation the protein scaffold is degraded and mineralization occurs via mineral deposition at the surfaces of the nascent crystallites until they almost completely fill the enamel volume. While the microstructure of enamel is organized by ameloblasts, enamel matrix protein assemblies exert exquisite control over mineral phase transformation, shape of the mineral particles and their structural organization at the nano- and mesoscales (Beniash et al., 2009; Margolis et al., 2006; Shin et al., 2020; Wald et al., 2017).

There are three major matrix proteins in secretory enamel – amelogenin, enamelin and ameloblastin. Amelogenin is the predominant enamel protein, comprising roughly 90% of the enamel matrix. It is a relatively hydrophobic modular protein that comprises an N-terminal Tyr-rich peptide (TRAP), a central Pro- and Glu-rich central domain, and a more hydrophilic C-terminus (Margolis et al., 2006). Amelogenin is an intrinsically disordered protein (Delak et al., 2009), which is soluble in acidic conditions and forms a hierarchical self-assembled gel at physiological pH (Beniash et al., 2012; Beniash et al., 2011; Nanci et al., 1998; Wiedemann-Bidlack et al., 2007). The amelogenin gene is located on sex chromosomes and only the AMELX gene located on the X chromosome encodes the functional version of this protein. Amelogenin plays a critical role in enamel biomineralization, and mutations in the AMELX gene cause X-linked Amelogenesis Imperfecta (AI), a congenital enamel disorder manifested by severe hypoplasia and hypomineralization and loss of enamel structural and functional integrity (Smith et al., 2017). The key role of this protein in enamel formation has been also confirmed by multiple studies of genetically modified animal models (Gibson et al., 2001; Hu et al., 2016; Pugach et al., 2010; Shin et al., 2020) and *in vitro* mineralization studies (Beniash et al., 2005; Kwak et al., 2009; Tao et al., 2018; Wiedemann-Bidlack et al., 2011). Typical biomineralization proteins are highly acidic and carry multiple phosphates (George and Veis, 2008). In contrast, amelogenin is a neutral protein and has only one phosphorylation site at Ser16, yet *in vitro* mineralization experiments demonstrate outsized importance of this single phosphate in stabilizing initially deposited amorphous calcium phosphate (ACP) and preventing its transformation into an apatitic crystalline phase (Kwak et al., 2009; Le Norcy et al., 2011; Tao et al., 2019; Wiedemann-Bidlack et al., 2011).

Recently, we generated a Ser16 to Ala substitution knock-in (KI) mouse model, in which amelogenin cannot be phosphorylated (Shin et al., 2020). The analysis of forming enamel in this model revealed that the rate of transformation of initially formed ACP to crystalline phase is higher compared to the wild type (WT), demonstrating that amelogenin phosphorylation controls phase transformation in this system. At the same time, this single amino acid substitution led to other, somewhat unexpected, phenotypic changes, including, reduced thickness of enamel, ectopic enamel surface calcification, the absence of ameloblast Tomes' processes, the loss of the characteristic enamel rod structure, and progressive ameloblast cell pathology. These results indicated that amelogenin phosphorylation has multiple functions in enamel biomineralization, in addition to its control over the rate of phase transformation. Here, we investigate how the lack of amelogenin phosphorylation affects the chemical composition and structural organization of mature enamel.

2. Materials and Methods.

2.1. Animal protocol approval

Animal care and use were carried out in accordance with protocols approved by the Institutional Animal Care and Use Committees at University of Pittsburgh, Division of Laboratory Animal Resources. The mice were housed in facilities approved by the Association for Assessment and Accreditation of Laboratory Animal Care.

2.2. Generation of KI mice lacking AMELX phosphorylation

The detailed description of the generation of KI mice was reported in a previous study (Shin et al., 2020). Briefly, gene-targeted KI mice carrying a point mutation (Ser-16 to Ala-16: AGC≫GCC; S16A) on exon 3 in the X-chromosomal AMELX gene from WT C57BL/6 genomic DNA were originally generated at ingenious Targeting Laboratory (Ronkonkoma, NY), and then, Neomycin-deleted AMELX-S16A heterozygous (HET) mice were transferred to the animal facilities at The Forsyth Institute (Cambridge, MA). HET mice were bred with C57Bl/6 mice to obtain WT male and females, HET females and KI male littermates. The colony was subsequently transferred to the University of Pittsburgh animal facilities where it is currently being maintained.

2.3. General sample preparation of WT, HET, and KI incisor enamel for photoemission electron microscopy (PEEM), scanning electron microscopy (SEM), Raman microspectroscopy and microhardness analysis.

Hemimandibles from adult WT, HET female, and KI male mice were dissected and the remaining soft tissues were removed by scraping. The specimens were then stored in 70% ethanol followed by dehydration through graded ethyl alcohol treatment. Specimens were then embedded in Epofix (Electron Microscopy Sciences, Hatfield, PA) in plastic molds. After the resin was fully cured (24–48 h), the embedded blocks were ground to expose planes of interest using a Minimet 1000 polisher (Buehler, Lake Bluff, IL) with progressively finer Carbomet PSA silicon carbide grinding paper (600, 800 and 1200 grit). For PEEM and microhardness analyses, the erupted portions of the incisors were ground and polished in the transverse plane of the incisor, while for SEM and Raman microspectroscopy the incisors were polished in the midsagittal plane. Griding progress was monitored using a dissecting microscope. Once the desired plane was exposed the samples were further polished using TexMet and MicroCloth lapping papers with progressively finer abrasive suspensions (6, 1, 0.25 μm). Samples were sonicated in ethanol between polishing cycles to remove larger abrasive particles and debris. The surface quality was monitored using a reflective light microscope. The final polished blocks were sonicated in ethanol for 10 min to remove any remaining debris and stored in dry conditions prior to use.

2.4. SEM analysis

For backscattered SEM (BS SEM) experiments the polished samples were carbon-coated using a Cressington carbon coater. The samples were studied using Jeol JSM-6335F microscope at the Center for Biological Imaging at the University of Pittsburgh. After collecting the BS SEM data, the samples were etched using 30% phosphoric acid for 10 sec. The samples were rinsed in distilled water and air dried. The samples were then coated with Au/Pd, using a Cressington Sputter Coater, and studied under the same microscope in secondary electron (SE SEM) mode. BS SEM microscopy was conducted at a 10 kV accelerating voltage and a 7 mm working distance. SE SEM microscopy was conducted at a 3 kV accelerating voltage and a 5 mm working distance.

2.5. Raman microspectroscopy analysis

Raman microspectroscopy was performed on the erupted portions of the incisors polished in the midsagittal plane. The microspectroscopy was conducted using a 488 nm laser at 50% power, with 10-sec exposure time per scan and 100 scans per spectrum. Incisors from three animals per genotype were analyzed. The analysis was performed using Renishaw inVia Raman microscope at the University of Pittsburgh Nanofabrication and Characterization Facility. Data analysis was conducted using Spectrum (Perkin-Elmer, Waltham, MA) and OriginPro 2016 (Origin Labs, Northampton, MA) software packages.

2.6. Microhardness analysis

Microhardness analysis was conducted on the erupted portions of incisors using a Micromet 2100 microhardness tester (Buehler, Lake Bluff, IL) with a 10 gf load and a 5-sec dwelling time. Incisors from 5 WT and 4 KI animals were tested. Ten indentations per animal were acquired and an average Vickers hardness value per animal was calculated. The results were analyzed and plotted using a GraphPad Prism software package.

2.7. PEEM analysis

The samples with exposed transverse planes prepared as described above were further processed by grinding using 1000 grit SiC paper (Buehler, Lake Bluff, IL) and polishing with 300 nm and then 50 nm alumina suspensions (Buehler, Lake Bluff, IL) using an Automet 250 polisher (Buehler, Lake Bluff, IL). All grinding and polishing solutions were prepared in 1 g/L calcium chloride solution to minimize dissolution of crystalline or any amorphous phases, if present. The polished samples were cleaned, air-dried, and coated in 1 nm Pt in the area of interest and 40 nm elsewhere while spinning and tilting (De Stasio et al., 2003; Frazer et al., 2004; Gilbert, 2014).

Polarization-dependent Imaging Contrast (PIC) mapping (DeVol et al., 2014; Metzler et al., 2008; Stifler et al., 2018) and component mapping (Nicholls et al., 2007; Schmidt et al., 2022) were performed using PhotoEmission Electron spectroMicroscopy (PEEM) (De Stasio et al., 1998), and specifically the PEEM3 instrument on beamline 11.0.1 at the Advanced Light Source (ALS) at Lawrence Berkeley National Lab. A stack of 38 images was acquired at 19 different x-ray polarizations from horizontal to vertical in 5° increments (Stifler et al., 2018), and two energies per polarization, +/-0.2 eV from the Ca L_2 peak position (352.6 eV), because the position varies with crystal orientations, and these two energies maximize contrast in PIC maps (Stifler et al., 2018). This acquisition mode induced minimal charging (Gilbert et al., 2000) and radiation damage The stacks of images were imported into the PeemVision software package and aligned when necessary, then the images acquired at 352.6 + 0.2 eV were digitally divided by the corresponding images acquired at 352.6 – 0.2 eV to increase the dichroic contrast, thus, reducing the stack to 19 images, one for each polarization. The 19-image stack was used to calculate PIC maps using the GG-macros 2021. The large area composite maps were created from an array of partly overlapping PIC maps that were blended in Adobe Photoshop® CC 2021 using the Auto-Blend Layers tool.

For component mapping experiments, the illuminating X-rays were circularly polarized, the sample voltage was − 18 kV. For calcium component mapping, stacks consisting of absorption images at a specific photon energy were acquired while scanning the photon energy across the Ca $L_{2,3}$-edge, from 340 to 360 eV, with steps of 0.1 eV between 345 and 355 eV, and steps of 0.5 eV elsewhere. Therefore, each pixel in a stack contains the full Ca $L_{2,3}$-edge spectrum. The fields of view of the stacks were set to 20 and 60 μm with 20 and 60-nm pixels, respectively. All stacks were aligned, if necessary, with the PEEMVision software.

We initially used ACP, low-crystallinity hydroxyapatite (LC-HAP), and hydroxyapatite (HAP) from Beniash et al. 2009 as the component reference spectra for the first round of component maps. As the Beniash et al. 2009 spectra were acquired on a different beamline and, thus, had dramatically different peak 1 to peak 3 intensity ratio, the Ca movies were only fit to a small energy range around peak 2. After this mapping, 130 single-pixel spectra at least 90% ACP, 500 single pixel spectra at least 98% LC-HAP, and 500 single pixel spectra that were at least 90% HAP and had intensity over 200 were extracted across 10 different stacks. All spectra for a single phase were aligned and then averaged. The ACP, LC-HAP, and HAP average spectra were all aligned to HAP and then rigidly shifted so that peak 1 for all three spectra was at 352.6 eV. After they were all aligned, a linear fit to pre-edge 342.6 eV and 346.19 eV was subtracted, and the spectra were normalized so that the area under the curve between 345 eV and 355 eV was 17. This value was selected because it resulted in HAP having a peak 1 intensity 1. These averaged spectra were used as components for mapping, which we call CAS3 (the CAS3 component spectra are provided as text files in the Supplementary data), with ACP, LC-HAP, and HAP being displayed as red, green, and blue, respectively. The CAS3 component spectra are provided as text files in the Supplement. The Ca distribution maps were created by averaging 7 images in the Ca stack in the post-edge centered at an energy of 357 eV and subtracting the average of 7 images in the pre-edge centered at 344 eV. All images were then leveled between 10 and 40. For Fig. 3A4-D4, only the pixels that contain more than 90% ACP or more were selected and displayed on top of the Ca distribution map. This was accomplished by selecting a pure red pixel in Adobe Photoshop® CC 2021 with the magic wand tool and a tolerance of 25, inverting the selection, and deleting everything else from the component map.

3. Results

3.1. Microstructural differences between WT, KI, and HET mature enamel

Consistent with our earlier study on the role of amelogenin phosphorylation (Shin et al., 2020) in enamel formation, mature incisal KI enamel completely lacks enamel rods (Fig. 1D-E, Supplementary figure 1) in stark contrast to WT enamel that features enamel rods organized into an exquisite decussating pattern, with alternating arrays of rods oriented at angles 60°-70° to the rods in adjacent arrays and surrounded by interrod enamel (Fig. 1A-C; Figure S1A,B). In KI enamel, an approximately 30 μm thick layer of enamel adjacent to the Dentino-Enamel Junction (DEJ) appears to be homogeneously mineralized (Fig. 1D,F, Figure S1E). In etched samples, this inner enamel had a layered appearance with the layers aligned parallel to the DEJ (Fig. 1E). The surface layer of KI enamel contained irregularly shaped aggregates with porous under-mineralized areas separating them (Fig. 1D,F, Figure S1E,F). When viewed in the BS SEM mode, the outer enamel aggregates are darker, suggesting that they are less mineralized than the inner enamel (Figure S1E,F). The heterozygote (HET) enamel has a mosaic appearance with rodless KI-like enamel and WT-like decussating enamel areas alternating (Fig. 1G and Figure S1C,D). Noticeably, the WT-like enamel next to the KI areas is less organized compared to areas away from the KI-like enamel.

3.2. PIC mapping reveals that in WT enamel crystal c-axes within each rod are co-oriented, but they do not always align with the rod axes

To measure the crystallographic organization of enamel nanocrystals, we used PIC mapping at the calcium L_2 peak, which measures the orientation of the *c*-axis of enamel crystallites in each pixel, and displays it in color over large areas, with a spatial resolution of 60 nm (Beniash et al., 2019; DeVol et al., 2014; Stifler et al., 2018). The vertical direction in all PIC maps in Fig. 2 is the same as the normal to the DEJ plane and 0° *c*-axis orientation (cyan) in the PIC maps, which makes it easier to determine *c*-axes directions of enamel rods and interrod in the

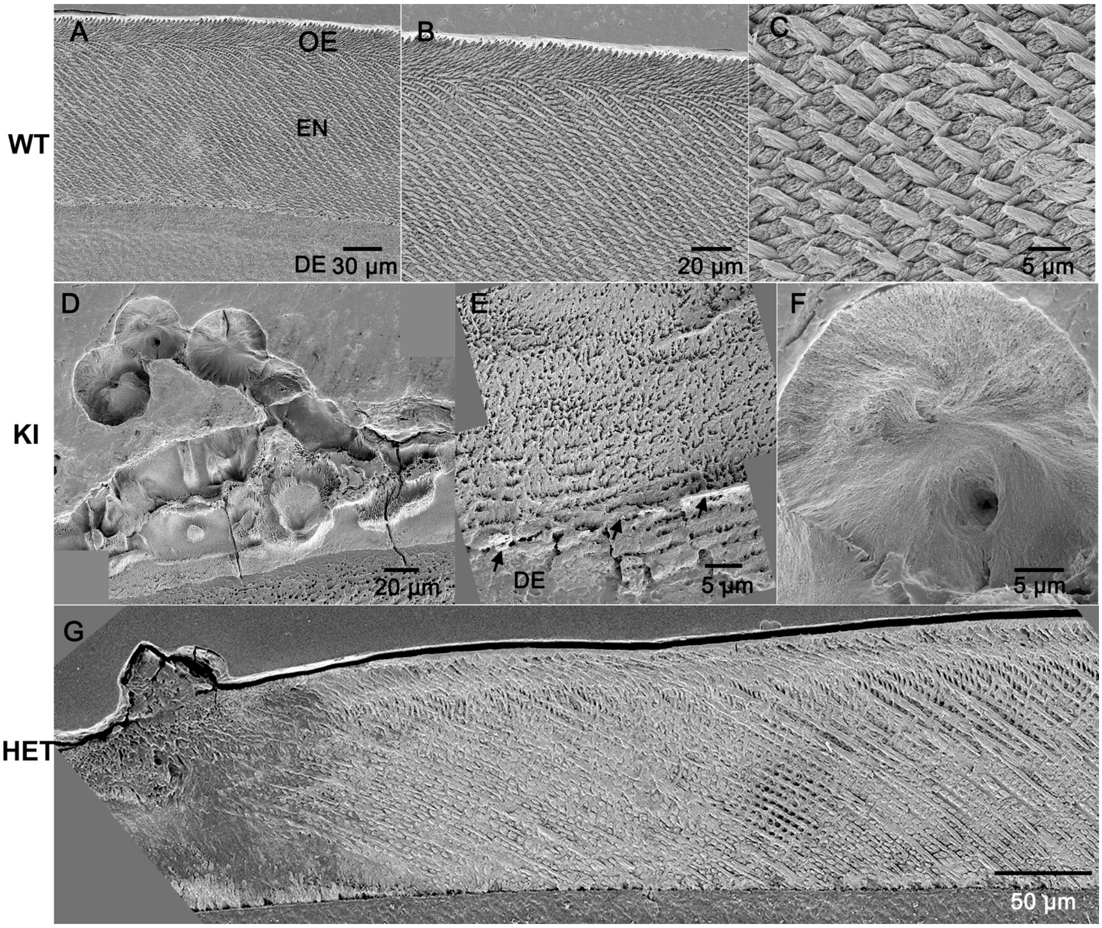

Fig. 1. SE SEM of etched erupted portions of enamel in WT (A-C), KI (D-F) and HET (G). A – low, B – intermediate and C – high magnification micrographs of the same region of WT enamel. The bulk of WT enamel (EN) comprises highly organized quasiorthogonal pattern of alternating rows of enamel rods with the interrod matter interwoven between the rods. The planes of enamel rods form right angle with the DEJ plane in the direction of the occlusal tip of the incisor (left). In the outer layer of enamel the rods change their direction and become more aligned with the plane of enamel surface. Note: the bright thin coating of the enamel surface is the iron-rich layer in A and B. DE- dentin. D. Low magnification micrograph of KI enamel. The inner portion of the etched enamel has a homogeneous appearance while the outer layer is highly disorganized with deep etched areas and patches of a highly porous matter. String of spherulites is attached to the enamel surface. E. Inner enamel layer adjacent to the dentino-enamel junction (DEJ) (arrows). F. A large magnification image of a spherulite. Note the radial etching pattern. G. HET enamel with KI-like area on the very left of the micrograph and WT-like area occupying the majority of the image. Note that some areas of the WT-like area are more soluble than others, based on the deeper etching profile.

maps. As expected, inside each rod in WT inner enamel the crystalline *c*-axes are generally co-oriented, with a small angle spread of ~ 10° (Fig. 2A-B). Throughout the bulk of WT enamel, *c*-axes are co-oriented inside all rods in each row, while the two alternating rows of rods have their *c*-axes at two distinct angles as shown in Fig. 2A,B where in one row of rods, the crystalline *c*-axes are oriented +30° (green) from the normal to the DEJ plane, and the other row of rods has the *c*-axes oriented + 60° (yellow), in other words the crystals' *c*-axes in the alternating rows of rods are 30° apart. Interrod crystals are oriented at −60° from the normal to the DEJ plane and are mostly co-oriented throughout the enamel thickness, within 30°. Note that the *c*-axis orientations of the rod crystals do not correspond with the rod elongation direction. In the bulk of incisal enamel the rod axes in the alternating rows are oriented at ±30-35° relative to the normal to the DEJ (60-70° apart) and inclined by about 30° toward the incisal tip (Warshawsky and Smith, 1971, Cox, 2013, Stifler et al., 2018). If *c*-axis orientations matched the rod elongation direction, the angles between crystalline *c*-axes in alternating rows of rods should both be 70°, but they are 30°. The crystals change orientation closer to the tooth surface, which corresponds to the change in the orientation of the rod axes in outer enamel (Fig. 1A,C). Moreover, the crystals within individual rods become less co-aligned in outer enamel. For instance, the crystals inside each rod are red and yellow (a 30° spread) in outer enamel instead of a single color near the DEJ and throughout all of the enamel thickness (Fig. 2A-C). Our analysis of the incisal enamel revealed that the angle between prevalent *c*-axes in alternating rows of rods varies. For example, rods in Fig. S2A are green and red, thus 60° apart.

3.3. KI mineral crystals become increasingly more misaligned with distance from the DEJ

In the inner KI enamel the distribution of the *c*-axes orientations is fairly homogeneous, with no particular patterns of crystal orientations in contrast to WT enamel, with its conspicuous decussating pattern. In KI, the *c*-axes of the crystals in the inner enamel layer are relatively co-oriented varying from 0° to + 30° from the normal to the DEJ plane (30° angle spread). The misalignment grows progressively further away from the DEJ in surface enamel, with the c-axes orientations varying from −30° to + 30° from the plane normal to the DEJ (60° angle spread).

3.4. HET enamel has regions of KI-like and WT-like enamel

The heterogeneity of HET enamel extends to its crystallography in addition to its microstructure. In the aprismatic regions, the *c*-axes vary

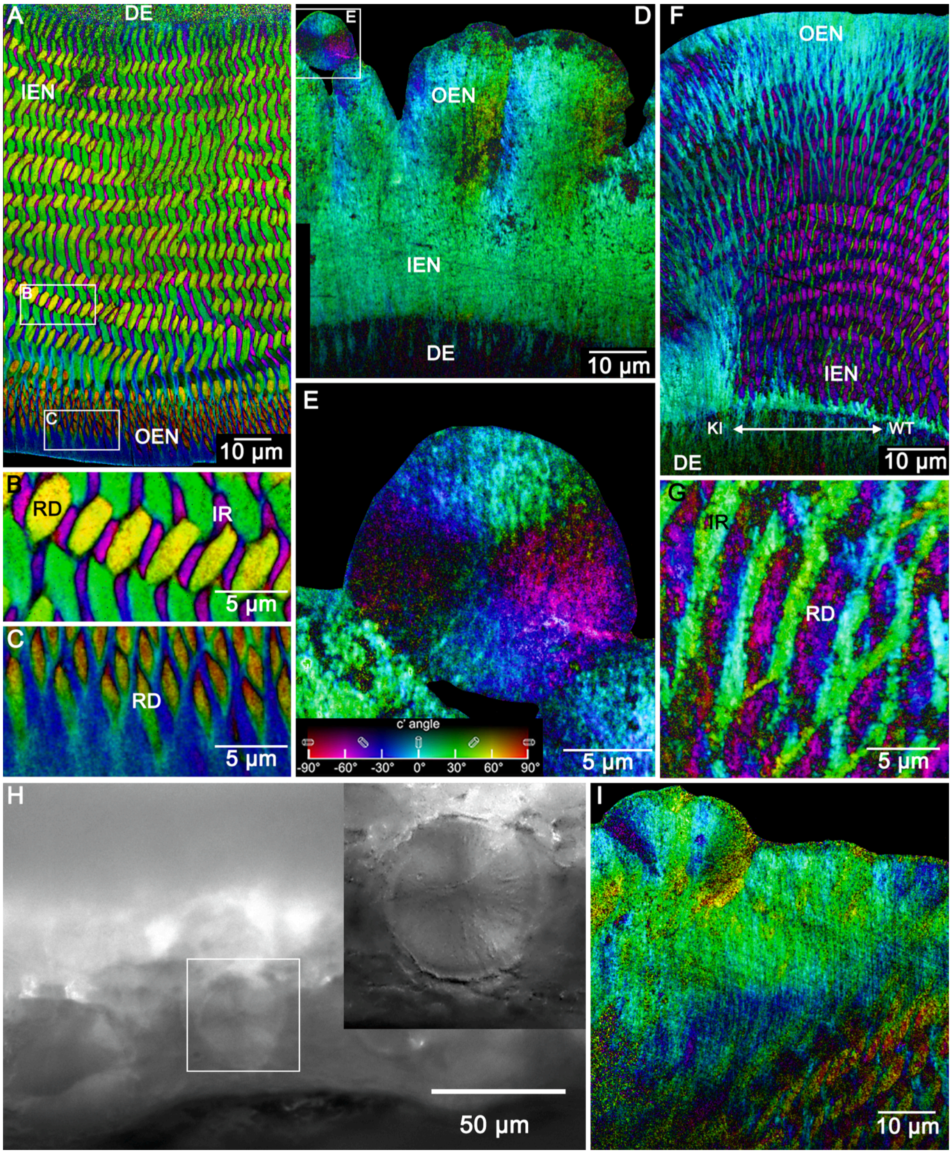

Fig. 2. A-G and I are PEEM PIC maps of WT, KI, and HET enamel. The key for the color-coding of *c*-axes orientations is in the lower left corner of panel E. A is low and B, C are high magnification maps of mature WT enamel as indicated by the white boxes in A. D. A map of KI enamel. E. Close up of the area in the white box in D containing a spherulite. F and G are low and high magnification maps of mature HET enamel. The double arrow in E indicates transition from WT-like to KI-like phenotype. H. Polarized light micrograph of a spherulite. The inset is the closeup of the boxed spherulite. I. Surface layer of HET enamel, with a spherulite attached to the enamel surface. The precise locations relative to the tooth cross-section are shown in Supplementary figure 4. DE - Dentin, IEN – inner enamel; OEN – Outer enamel; IR – interrod, R – rod.

gradually from −30° to + 30° (blue to cyan to green) with respect to the normal to the DEJ plane, as they do in KI enamel (Fig. 2F). However, the WT-like regions of decussating enamel in HET have substantial differences in crystal orientations. Although the overall decussating pattern is confined to the WT-like regions, the shapes of the rods and the interrod and the crystallographic co-orientation within each rod and with respect to the interrod are affected. Specifically, the rod and interrod boundaries appeared less sharp and more convoluted than in the WT. In the teeth we analyzed in PEEM, the local misorientation within both rod and interrod areas in HET enamel is significantly greater compared to either WT or KI enamel (Fig. 2G, Supplementary figure 3). The texture of enamel rod and interrod mineral appeared grainy with sharp differences in crystal orientations in the adjacent regions (Fig. 2G, 4C1,D1). In addition, the crystallographic disorganization of the rods gradually worsened with proximity to the KI-like areas (Fig. 2F-G, Supplementary figure 2B).

3.5. Spherulites in KI and HET enamel

The outermost mineral in KI enamel consists of regularly shaped spherical mineral particles which are partially or completely detached from the enamel layer (Fig. 1D,F, and Figure S1E). In BS SEM, they are brighter than the aggregates in the outer enamel layer and comparable to the inner enamel, indicating that they are more densely mineralized (Figure S1E). Upon etching, they exhibit the radial etching pattern similar to abiotic mineral spherulites, pointing to a probable reduction of biological control over mineralization in these structures. PIC mapping confirms that the partially detached spheres in KI enamel are indeed spherulites, with crystal orientations gradually changing around the sphere (Fig. 2E) (Olson et al., 2013; Sun et al., 2017). HET teeth analyzed with PIC mapping also contain a partial spherulite (Fig. 2I, Figure S1C). Polarized light microscopy also confirms that the detached spherical particles are indeed spherulites as they exhibit the characteristic Maltese cross pattern, which is enlarged in the inset (Fig. 2H). The angle spread of *c*-axes within each spherulite is 90°.

3.6. Mineral phases in WT, HET, and KI enamel

3.6.1. Component mapping reveals amorphous calcium phosphate (ACP) in WT, HET, and KI mature enamel

Component mapping, using ACP, LC-HAP, and HAP component spectra at the Ca L-edge, reveals that in all genotypes there is ACP in addition to apatite in mature enamel. In the WT, there are only small patches of ACP, primarily localized in the interrod (Fig. 3A3). KI enamel contains more ACP than WT, and ACP is distributed throughout the KI enamel (Fig. 3B3). One HET region that was acquired on the part of the tooth that has minimal defects and well defined WT-like rods , contains slightly more ACP than WT and about the same amount of ACP as KI (Fig . 3C3), whereas another region in HET acquired on a visibly defective section of tooth (Fig. 3D3), contains the most ACP out of all regions analyzed in all samples. Both HET regions have ACP localized to the interrod, as in the WT, but more of it. Comparing single pixel spectra from each phase and from each genotype to previously published spectra (Beniash et al., 2009), it is clear that all three phases are present and are not an artifact of 3-component fitting (Fig. 4A-C). Comparing spectra, obtained from over 100 single pixels from either WT rods, WT interrod, or KI aprismatic enamel, and averaged, WT rod enamel is the closest to pure HAP, followed by KI aprismatic enamel. WT interrod enamel has a much less intense spectrum and a similar shape to the ACP spectrum, consistent with ACP localization in the interrod.

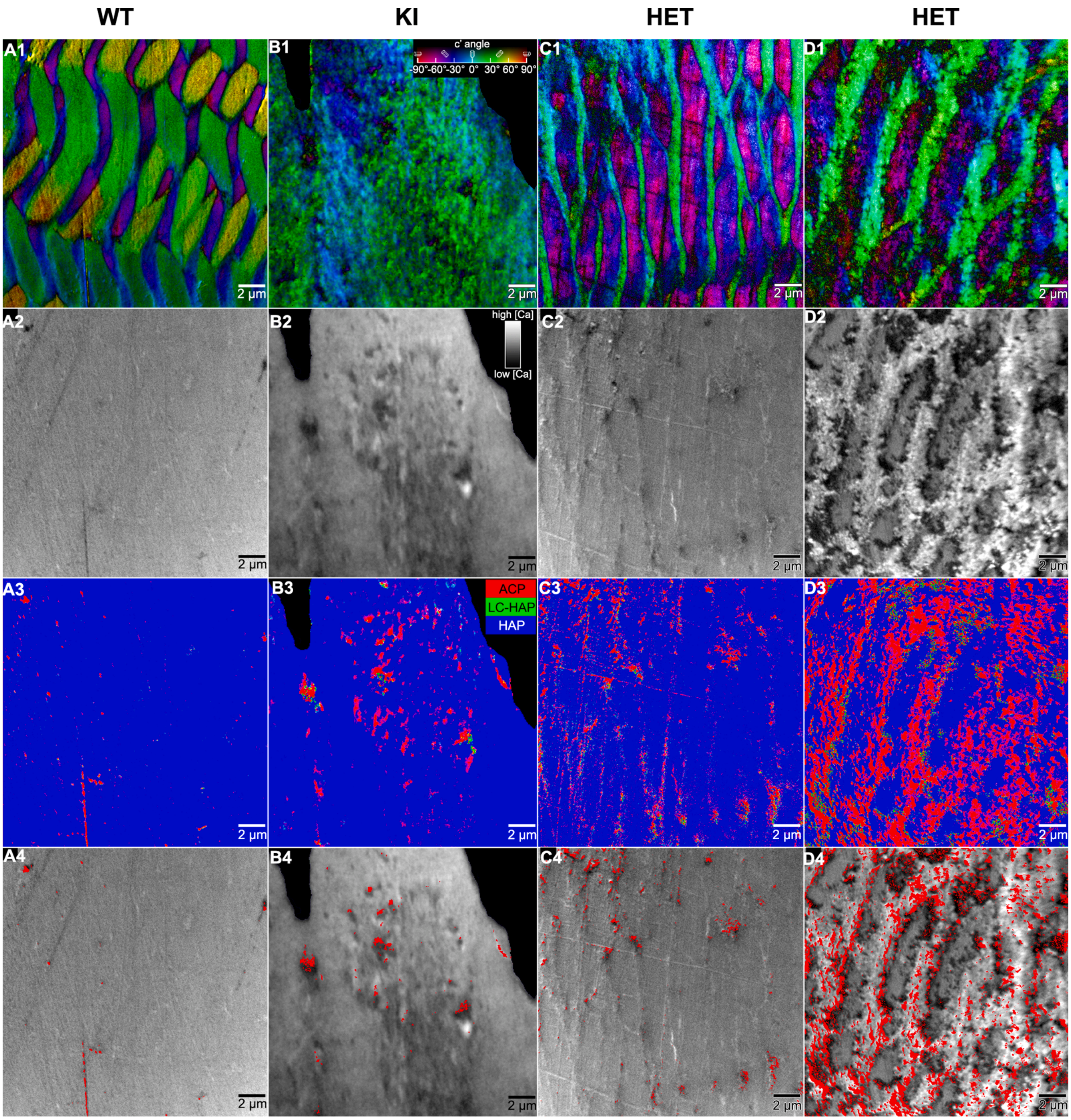

Fig. 3. A WT, B KI C minimally defective HET, and D extensively defective HET mouse enamel PIC maps (A1-D1), calcium distribution maps (A2-D2), component maps (A3-D3), and pixels from component maps containing a least 90% Amorphous Calcium Phosphate (ACP) overlaid on the calcium distribution maps (A4-D4). PIC maps show the morphology and crystal orientations of rods and interrod in WT and HET enamel and the aprismatic KI enamel according to the color bar in B1. Calcium distribution maps of the corresponding areas indicate where calcium concentration is higher or lower in the enamel. Component maps indicate the mineral phases detected in each 20-nm pixel and displayed in colors according to the color legend in B3: RGB are ACP, Low Crystallinity-HydroxyAPatite (LC-HAP), and HydroxyAPatite (HAP), respectively. A1-A4 WT mouse enamel is mainly comprised of HAP with distinct areas of ACP concentrated in the interrod. B1-B4 KI mouse enamel has no rods (aka prisms), thus it can all be considered “aprismatic” enamel, and shows a number of areas of ACP throughout. C1-C4 HET mouse enamel has more ACP in the interrod compared to WT enamel. D1-D4 HET in a different region of the same tooth in C1-C4, but with much more ACP, all localized in the interrod. In all panels, pixels that contain ACP in component maps appear black in PIC maps and calcium distribution maps, consistent with no crystallinity. The precise locations of these 4 areas relative to the tooth cross-section are shown in Fig. S4.

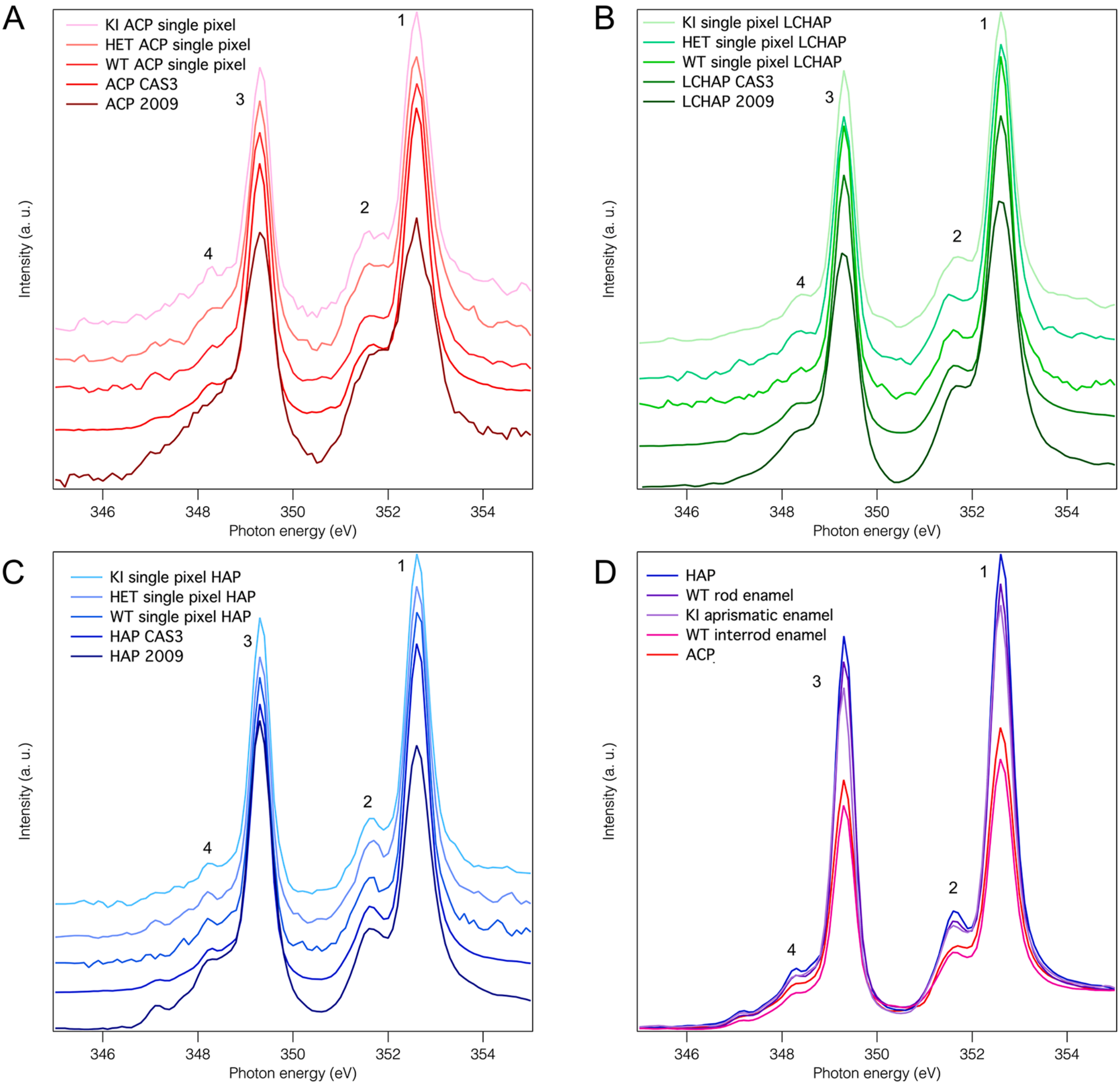

Fig. 4. Spectra from reference standards of ACP, LCHAP, HAP (from Beniash et al., 2009), the component spectra, CAS3, for ACP, LCHAP, HAP, extracted from mouse enamel and used for the component maps in Fig. 2 and single-pixel spectra extracted from WT, HET, and KI enamel for each of the three phases, A-C respectively. D Averaged spectra extracted from only the rod or interrod regions in WT and HET and aprismatic enamel in KI. The WT rod spectrum is mostly HAP, but peak 2 is not as sharp in the WT rod spectrum as it is in the HAP reference spectrum. KI aprismatic enamel is also mostly HAP, but peak 2 is even less sharp than in WT rod or HAP reference spectra, suggesting that KI aprismatic enamel is slightly more disordered than WT rod enamel. WT interrod has a low peak 1 intensity reminiscent of the ACP reference spectrum, but peak 2 is sharper than the ACP reference suggesting that WT interrod is a mixture of ACP and HAP.

3.6.2. Raman microspectroscopy reveals that mature KI enamel is more carbonated than WT enamel

Raman microspectroscopy results indicate that the mineral phase in mature KI enamel contains significantly more carbonate that WT, as shown in Fig. 5A,B, based on the increased intensity of the peak at 1071 cm^{-1}, which is associated with CO_3^{2-} ν_1 and PO_4^{3-} ν_1 bands (Awonusi et al., 2007; Penel et al., 1998; Xu et al., 2012). The height ratio between this peak and the major phosphate peak at 960 cm^{-1} is 1.6 times higher in KI enamel than in WT enamel (0.06 ± 0.006 vs 0.038 ± 0.0023; $p = 0.0004$), suggesting that the carbonate content in KI enamel is between 6 and 8%. Several differences between the spectra are also apparent in the PO_4^{3-} ν_2 and ν_4 regions (400 – 450 and 550–650 cm^{-1} respectively), however, these differences are hard to interpret.

3.6.3. Enamel is harder in WT than in KI

Microindentation tests show a five-fold reduction in microhardness in KI vs. WT enamel: HV = 51.21 SD = 15.21 vs. HV = 259.8 SD = 10.01, respectively (Fig. 5C). This difference is highly significant, with $p < 0.0001$.

4. Discussion

Previously, we demonstrated that amelogenin phosphorylation plays critical roles in both early and late stages of enamel formation and affects not only extracellular events but also ameloblast cell biology (Shin et al., 2020). In the present study, we explore the effects of amelogenin phosphorylation on the crystallographic organization, mineral composition, and microhardness of mature enamel. Our main conclusion is that the lack of amelogenin phosphorylation is associated with a reduction in

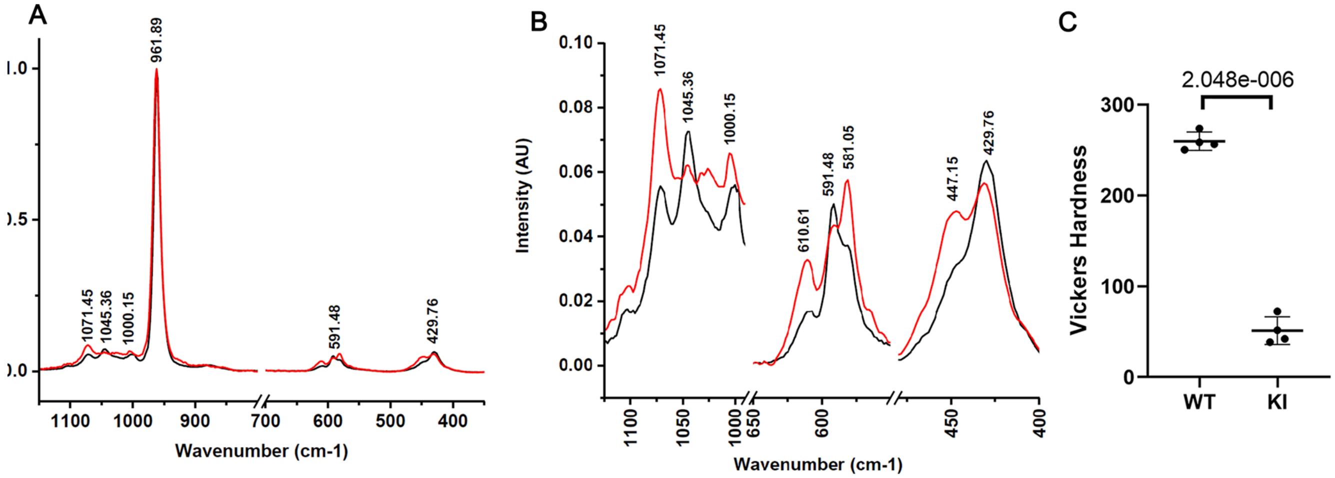

Fig. 5. A, B Representative Raman spectra taken from WT (black) and KI (red) mature incisal enamel. A. A spectral region containing major differences between WT and KI enamel from 1200 to 400 cm-1. B. A close up view of the three regions with most prominent differences. The most prominent and important difference is in 1071 cm-1 band, indicating an increase in carbonate level. There are also change in phosphate vibration regions at 620 – 570 cm-1 and 500 – 400 cm-1. C. Box plot of Vickers Hardness values for WT and KI erupted incisal enamel.

the biological control over the enamel mineralization processes.

Decussating incisal inner enamel consists of alternating rows of enamel rods running from the DEJ to the enamel surface. In the transverse plane the rods in alternating rows run in opposite directions at 70° from each other or ± 35° from the midsagittal plane (Cox, 2013) and lean toward the incisal tip at ~30-40° angle (Baldassarri et al., 2008; Stifler et al., 2018; Warshawsky and Smith, 1971). The observed high degree of alignment of *c*-axes of enamel crystals within the rods is in perfect agreement with our earlier study, where the incisal enamel was mapped in midsagittal plane (Stifler et al., 2018). Here, the enamel was mapped in the transverse plane, which better displays difference between the orientation of *c*-axes inside the rods and the long axes of the crystals, which do not always co-align with the long axes of the rods. Specifically, we found that the *c*-axes in alternating rods are only 30° apart – green/yellow in Fig. 2A and not the expected 70°, which would be observed if the *c*-axes were aligned with the long axes of the crystals. The rods maintain these crystallographic relationships throughout the thickness of inner enamel, illustrating the exquisite level of control and coordination of the mineral organization and crystallography by the ameloblasts.

The apatite nanocrystals of KI enamel in the first 30 μm from the DEJ are elongated roughly along the normal to the DEJ plane (Shin et al., 2020), whereas their *c*-axes are oriented at 0° to + 30° from the normal to the DEJ plane, as observed here with PIC mapping. In inner KI enamel, the lack of enamel rods and decussating pattern indicates a significant reduction of biological control in this region. The outer enamel maintains this general crystallographic orientation of the enamel crystals, but it varies gradually from + 30° to −30°, thus the spread of the *c*-axes orientations is broader (60°) than in inner enamel, indicating decreasing control with distance from the DEJ. Finally, the outermost layer of KI mineral contains spherulites, with angle spread of 90°, that are fully or partially detached from the outer enamel layer. These observations, combined, demonstrate a progressive reduction in biological control over mineralization from the DEJ to outer enamel.

HET enamel often has a mosaic appearance with areas of rodless enamel similar to KI enamel and other areas, which have a fairly organized decussating pattern, similar to that seen in the WT. Formation of clusters of cells expressing different-chromosome alleles is a well-recognized biological process known as X-inactivation or “lyonization”, named after Mary Lyon, who discovered this phenomenon (Harper, 2011; Lyon, 1961). In this process in females one of the X-chromosome alleles is randomly and permanently silenced in a cell early in the development and all the descendants of this cell will have the same allele silenced. This implies that some clusters or patches of ameloblasts will express WT amelogenin, while other clusters will express KI amelogenin. This phenomenon was described in the female patients with X-linked Amelogenesis imperfecta, caused by mutations in AMELX gene (Hart et al., 2002; Patel et al., 1991; Sauk Jr et al., 1972; Wright, 2006). Interestingly, the organization of enamel crystals in the rods and the interrod in WT-like regions in HET enamel, in which cells presumably express the WT allele, were more misoriented than in the WT. Although the sample size is very small, this may suggest that mutated amelogenin not only affects mineralization in direct proximity to the ameloblasts expressing the mutant allele, but it can also influence the orientation of crystals growing in regions where amelogenin is phosphorylated, resulting in enamel crystals in decussating rods that are more misoriented in HET enamel than in WT enamel.

At this point we can only surmise what is the basis of these long-range effects. One potential explanation is that the non-phosphorylated amelogenin alters the physicochemical conditions in the extracellular space. We have previously shown that in the absence of amelogenin phosphorylation the ACP-carbonated apatite phase transformation in developing enamel is accelerated (Shin et al., 2020). This faster transformation may lead to acidification of the extracellular environment not only in close proximity to cells secreting non-phosphorylated amelogenin, but also in surrounding areas, potentially leading to long-range effects. The fact that the organization of WT-like enamel in proximity to KI-like areas is worse than at a distance supports this notion. Another clue pointing toward the role of phosphorylated amelogenin in maintaining the chemistry of the extracellular environment, is the significant increase in carbonate content in mature enamel mineral, determined by Raman microspectroscopy. pH balance in the forming enamel is under tight biological control (Smith et al., 1996) which is maintained via regulation of carbonate/bicarbonate system by carbonic anhydrases and other molecules (Lacruz et al., 2010; Yin and Paine, 2017). Acidification due to faster mineral phase transformation potentially can throw the system off balance and leads to a higher carbonate concentration in the enamel fluid and thus to increased carbonate content in enamel crystals (Tadic et al., 2002). Furthermore, decreased control over mineralization also leads to worsening of the material properties of enamel as evidenced by our microhardness results.

The observed presence and distribution of ACP in mature WT, KI, and HET enamel may be of particular interest. The ACP that we observe in mature enamel is consistent with the observation of intragranular ACP in WT rodent enamel using atom probe tomography (Gordon et al., 2015). As discussed by these authors, the presence and type of ACP observed (*i.e.*, Mg-substituted ACP found in unpigmented enamel vs. a mixture of ferrihydrite and amorphous iron-calcium phosphate in pigmented enamel) can have a dramatic effect on enamel properties. In the present study, all three genotypes contained ACP, which was predominantly localized in the interrod in WT and WT-like HET enamel. As shown in Fig. 3D4, the greatest amounts of ACP were observed in the interrod of HET enamel. In contrast, KI enamel exhibits ACP regions throughout its aprismatic enamel layer that lacks the rod structure. Although we have demonstrated that amelogenin phosphorylation significantly affects the rate of ACP transformation to apatitic enamel crystals during the secretory stage of enamel formation (Shin et al., 2020), we currently do not have any information on the direct effect of amelogenin phosphorylation on the regulation of mineral phase formation and transformation in the maturation stage during which enamel proteins are removed and the bulk of enamel mineral is deposited. In addition, in KI enamel, ameloblasts undergo progressive cell pathology throughout enamel development. For these reasons, additional studies are needed to fully understand our current findings on the presence and distribution of ACP in KI and HET enamel.

The presence of spherulites, another indicator of unregulated crystallization, could also result from ACP accumulation. Large clusters of unorganized ACP aggregating at and around the surface in KI and KI-like regions of HET enamel are likely responsible for the formation of spherulites, which readily form from amorphous aggregates in many different systems (Al-Atar et al., 2010; Fowler et al., 2002; Geveling and Maslenkov, 1976; Hincke et al., 2012; Parmentier et al., 2007; Péloquin et al., 1996). Collectively, our results demonstrate that phosphorylated amelogenin plays a critical role in controlling mineralization, mineral phase, crystal organization, and the crystallographic orientation in mature mouse enamel.

5. Conclusions

Lack of amelogenin phosphorylation leads to a progressive loss of control over mineralization, manifested by the lack of rods and decussation in KI enamel, stark differences in structural organization and crystallographic orientation of enamel crystals between WT and KI enamel, and by the presence of spherulites in KI enamel. These results lead us to the conclusion that the single phosphorylation of amelogenin plays an outsized role in not only the structural organization of enamel, but also strongly influences specific crystallographic, biomechanical and chemical characteristics of dental enamel.

CRediT authorship contribution statement

Cayla A. Stifler: Investigation, Formal analysis, Writing – original draft, Writing – review & editing, Visualization. **Hajime Yamazaki:** Investigation, Formal analysis, Writing – review & editing, Visualization. **Pupa U.P.A. Gilbert:** Supervision, Funding acquisition, Investigation, Writing – original draft, Writing – review & editing. **Henry C. Margolis:** Conceptualization, Supervision, Project administration, Funding acquisition, Writing – review & editing. **Elia Beniash:** Conceptualization, Supervision, Project administration, Funding acquisition, Investigation, Writing – original draft, Writing – review & editing, Visualization.

Declaration of Competing Interest

The authors declare that they have no known competing financial interests or personal relationships that could have appeared to influence the work reported in this paper.

Acknowledgements

This study was supported by a grant R01 DE029211 from the National Institutes of Health/National Institute of Dental and Craniofacial Research to H.C.M. and E.B. P.U.P.A.G. received 40% support from DOE–BES–Chemical Sciences, Geosciences, Biosciences–Geosciences Grant DEFG02-07ER15899, 40% support from the Laboratory Directed Research and Development (LDRD) program at Berkeley Lab, through DOE-BES, under Award Number DE-AC02-05CH11231, and 20% support from NSF Biomaterials Grant DMR-1603192. All PEEM experiments were done at the Advanced Light Source (ALS), which is supported by the Director, Office of Science, Office of Basic Energy Sciences, US Department of Energy under Contract No. DE-AC02-05CH11231. The authors thank Mr. Jonathan Franks and the Centre for Biological Imaging at the University of Pittsburgh for their expert support of our SEM studies and Dr. Daniel Lamont and the Nanofabrication and Nanocharacterization Facility at the University of Pittsburgh Swanson School of Engineering for their help with Raman microspectroscopy.

Appendix A. Supplementary data

Supplementary data to this article can be found online at https://doi.org/10.1016/j.jsb.2022.107844.

References

Al-Atar, U., Bokov, A.A., Marshall, D., Teichman, J.M.H., Gates, B.D., Ye, Z.-G., Branda, N.R., 2010. Mechanism of calcium oxalate monohydrate kidney stones formation: layered spherulitic growth. Chem. Mater. 22 (4), 1318–1329.

Awonusi, A., Morris, M.D., Tecklenburg, M.M.J., 2007. Carbonate assignment and calibration in the Raman spectrum of apatite. Calcif Tissue Int 81 (1), 46–52.

Bajaj, D., Arola, D.D., 2009. On the R-curve behavior of human tooth enamel. Biomaterials 30 (23-24), 4037–4046.

Baldassarri, M., Margolis, H.C., Beniash, E., 2008. Compositional determinants of mechanical properties of enamel. J Dent Res 87 (7), 645–649.

Beniash, E., Simmer, J.P., Margolis, H.C., 2005. The effect of recombinant mouse amelogenins on the formation and organization of hydroxyapatite crystals in vitro. J Struct Biol 149 (2), 182–190.

Beniash, E., Simmer, J.P., Margolis, H.C., 2012. Structural Changes in Amelogenin upon Self-assembly and Mineral Interactions. J Dent Res 91 (10), 967–972.

Beniash, E., Metzler, R.A., Lam, R.S.K., Gilbert, P.U.P.A., 2009. Transient amorphous calcium phosphate in forming enamel. J Struct Biol 166 (2), 133–143.

Beniash, E., Deshpande, A.S., Fang, P.A., Lieb, N.S., Zhang, X., Sfeir, C.S., 2011. Possible role of DMP1 in dentin mineralization. J Struct Biol 174 (1), 100–106.

Beniash, E., Stifler, C.A., Sun, C.-Y., Jung, G.S., Qin, Z., Buehler, M.J., Gilbert, P.U.P.A., 2019. The hidden structure of human enamel. Nat. Commun. 10, 4383.

Chai, H., Lee, J.- J.-W., Constantino, P.J., Lucas, P.W., Lawn, B.R., 2009. Remarkable resilience of teeth. Proc Natl Acad Sci U S A 106 (18), 7289–7293.

Cox, B.N., 2013. How the tooth got its stripes: patterning via strain-cued motility. J R Soc Interface 10 (84), 20130266. https://doi.org/10.1098/rsif.2013.0266.

De Stasio, G., Capozi, M., Lorusso, G.F., Baudat, P.A., Droubay, T.C., Perfetti, P., Margaritondo, G., Tonner, B.P., 1998. MEPHISTO: Performance Tests of a Novel Synchrotron Imaging Photoelectron Spectromicroscope. Rev. Sci. Instrum. 69, 2062–2067.

De Stasio, G., Frazer, B.H., Gilbert, B., Richter, K.L., Valley, J.W., 2003. Compensation of charging in X-PEEM: a successful test on mineral inclusions in 4.4 Ga old zircon. Ultramicroscopy 98 (1), 57–62.

Delak, K., Harcup, C., Lakshminarayanan, R., Sun, Z., Fan, Y., Moradian-Oldak, J., Evans, J.S., 2009. The tooth enamel protein, porcine amelogenin, is an intrinsically disordered protein with an extended molecular configuration in the monomeric form. Biochem. 48 (10), 2272–2281.

DeVol, R.T., Metzler, R.A., Kabalah-Amitai, L., Pokroy, B., Politi, Y., Gal, A., Addadi, L., Weiner, S., Fernandez-Martinez, A., Demichelis, R., Gale, J.D., Ihli, J., Meldrum, F. C., Blonsky, A.Z., Killian, C.E., Salling, C.B., Young, A.T., Marcus, M.A., Scholl, A., Doran, A., Jenkins, C., Bechtel, H.A., Gilbert, P.U.P.A., 2014. Oxygen spectroscopy and polarization-dependent imaging contrast (PIC)-mapping of calcium carbonate minerals and biominerals. J Phys Chem B 118 (28), 8449–8457.

Fowler, A., Prokoph, A., Stern, R., Dupuis, C., 2002. Organization of oscillatory zoning in zircon: analysis, scaling, geochemistry, and model of a zircon from Kipawa, Quebec, Canada. Geochim Cosmochim Acta 66 (2), 311–328.

Frazer, B.H., Girasole, M., Wiese, L.M., Franz, T., Stasio, G.D., 2004. Spectromicroscope for the Photoelectron Imaging of Nanostructures with X-rays (SPHINX): performance in biology, medicine and geology. Ultramicroscopy 99 (2-3), 87–94.

George, A., Veis, A., 2008. Phosphorylated proteins and control over apatite nucleation, crystal growth, and inhibition. Chem Rev 108 (11), 4670–4693.

Geveling, N.N., Maslenkov, S.B., 1976. Solidification of eutectic Ni-Ni 3 Ti alloys. Met. Sci. Heat Treat. 18 (9), 755–760.

Gibson, C.W., Yuan, Z.-A., Hall, B., Longenecker, G., Chen, E., Thyagarajan, T., Sreenath, T., Wright, J.T., Decker, S., Piddington, R., Harrison, G., Kulkarni, A.B., 2001. Amelogenin-deficient mice display an amelogenesis imperfecta phenotype. J Biol Chem 276 (34), 31871–31875.

Gilbert, B., Andres, R., Perfetti, P., Margaritondo, G., Rempfer, G., De Stasio, G., 2000. Charging phenomena in PEEM imaging and spectroscopy. Ultramicroscopy 83 (1-2), 129–139.

Gilbert, P.U.P.A., 2014. Photoemission spectromicroscopy for the biomineralogist. In: DiMasi, E., Gower, L.B. (Eds.), Biomineralization Sourcebook. CRC Press, Boca Raton, FL, Characterization of Biominerals and Biomimetic Materials, pp. 135–151.

Gordon, L.M., Cohen, M.J., MacRenaris, K.W., Pasteris, J.D., Seda, T., Joester, D., 2015. Amorphous intergranular phases control the properties of rodent tooth enamel. Science 347 (6223), 746–750.

Harper, P.S., 2011. Mary Lyon and the hypothesis of random X chromosome inactivation. Hum Genet 130 (2), 169–174.

Hart, P.S., Aldred, M.J., Crawford, P.J.M., Wright, N.J., Hart, T.C., Wright, J.T., 2002. Amelogenesis imperfecta phenotype-genotype correlations with two amelogenin gene mutations. Arch Oral Biol 47 (4), 261–265.

Hincke, M.T., Nys, Y., Gautron, J., Mann, K., Rodriguez-Navarro, A.B., McKee, M.D., 2012. The eggshell: structure, composition and mineralization. Front Biosci 17, 1266–1280.

Hu, Y., Smith, C.E., Cai, Z., Donnelly, L.A., Yang, J., Hu, J.C., Simmer, J.P., 2016. Enamel ribbons, surface nodules, and octacalcium phosphate in C57BL/6 Amelx(-/-) mice and Amelx(+/-) lyonization. Mol Genet Genomic Med 4, 641–661.

Kwak, S.-Y., Wiedemann-Bidlack, F.B., Beniash, E., Yamakoshi, Y., Simmer, J.P., Litman, A., Margolis, H.C., 2009. Role of 20-kDa Amelogenin (P148) Phosphorylation in Calcium Phosphate Formation in Vitro. J Biol Chem. 284 (28), 18972–18979.

Lacruz, R.S., Hilvo, M., Kurtz, I., Paine, M.L., 2010. A survey of carbonic anhydrase mRNA expression in enamel cells. Biochem Biophys Res Commun 393 (4), 883–887.

Le Norcy, E., Kwak, S.-Y., Allaire, M., Fratzl, P., Yamakoshi, Y., Simmer, J.P., Margolis, H.C., 2011. Effect of phosphorylation on the interaction of calcium with leucine-rich amelogenin peptide. Eur J Oral Sci. 119, 97–102.

Lyon, M.F., 1961. Gene action in the X-chromosome of the mouse (Mus musculus L.). Nature 190 (4773), 372–373.

Maas, M.C., Dumont, E.R., 1999. Built to last: The structure, function, and evolution of primate dental enamel. Evol Anthropol. 8 (4), 133–152.

Margolis, H.C., Beniash, E., Fowler, C.E., 2006. Role of Macromolecular Assembly of Enamel Matrix Proteins in Enamel Formation. J Dent Res 85 (9), 775–793.

Metzler, R.A., Zhou, D., Abrecht, M., Chiou, J.-W., Guo, J., Ariosa, D., Coppersmith, S.N., Gilbert, P.U.P.A., 2008. Polarization-dependent imaging contrast in abalone shells. Phys Rev B 77 (6). https://doi.org/10.1103/PhysRevB.77.064110.

Nanci, A., Zalzal, S., Lavoie, P., Kunikata, M., Chen, W.-Y., Krebsbach, P.H., Yamada, Y., Hammarström, L., Simmer, J.P., Fincham, A.G., Snead, M.L., Smith, C.E., 1998. Comparative immunochemical analyses of the developmental expression and distribution of ameloblastin and amelogenin in rat incisors. J Histochem Cytochem 46 (8), 911–934.

Nicholls, M.A., Najman, M.N., Zhang, Z., Kasrai, M., Norton, P.R., Gilbert, P.U.P.A., 2007. The Contribution of XANES Spectroscopy to Tribology. Can. J. Chem. 85, 816–830. https://doi.org/10.1139/v07-093.

Nishikawa, S., 2017. Cytoskeleton, intercellular junctions, planar cell polarity, and cell movement in amelogenesis. J Oral Biosci 59 (4), 197–204.

Olson, I.C., Metzler, R.A., Tamura, N., Kunz, M., Killian, C.E., Gilbert, P.U.P.A., 2013. Crystal lattice tilting in prismatic calcite. J Struct Biol 183 (2), 180–190.

Parmentier, E., Cloots, R., Warin, R., Henrist, C., 2007. Otolith crystals (in Carapidae): Growth and habit. J Struct Biol 159 (3), 462–473.

Patel, R.-R., Hovijitra, S., Kafrawy, A.H., Bixler, D., 1991. X-linked (recessive) hypomaturation amelogenesis imperfecta: a prosthodontic, genetic, and histopathologic report. J Prosthet Dent 66 (3), 398–402.

Péloquin, A., Verpaelst, P., Ludden, J., 1996. Spherulitic rhyolites of the Archean Blake River Group, Canada; implications for stratigraphic correlation and volcanogenic massive sulfide exploration. Econ Geol 91, 343-354.

Penel, G., Leroy, G., Rey, C., Bres, E., 1998. MicroRaman spectral study of the PO4 and CO3 vibrational modes in synthetic and biological apatites. Calcif Tissue Int 63 (6), 475–481.

Pugach, M.K., Li, Y., Suggs, C., Wright, J.T., Aragon, M.A., Yuan, Z.A., Simmons, D., Kulkarni, A.B., Gibson, C.W., 2010. The amelogenin C-terminus is required for enamel development. J Dent Res 89 (2), 165–169.

Sauk Jr, J., Lyon, H.W., Witkop Jr, C., 1972. Electron optic microanalysis of two gene products in enamel of females heterozygous for X-linked hypomaturation amelogenesis imperfecta. Am J Hum Genet 24, 267.

Schmidt, C.A., Stifler, C.A., Luffey, E.L., Fordyce, B.I., Ahmed, A., Barreiro Pujol, G., Breit, C.P., Davison, S.S., Klaus, C.N., Koehler, I.J., LeCloux, I.M., Matute Diaz, C., Nguyen, C.M., Quach, V., Sengkhammee, J.S., Walch, E.J., Xiong, M.M., Tambutté, E., Tambutté, S., Mass, T., Gilbert, P.U.P.A., 2022. Faster crystallization during coral skeleton formation correlates with resilience to ocean acidification. J. Am. Chem. Soc. 144, 1332–1341. https://doi.org/10.1021/jacs.1c11434.

Shin, N.-Y., Yamazaki, H., Beniash, E., Yang, X.u., Margolis, S.S., Pugach, M.K., Simmer, J.P., Margolis, H.C., 2020. Amelogenin phosphorylation regulates tooth enamel formation by stabilizing a transient amorphous mineral precursor. J. Biol. Chem. 295 (7), 1943–1959.

Smith, C.E., Issid, M., Margolis, H.C., Moreno, E.C., 1996. Developmental Changes in the pH of Enamel Fluid and Its Effects On Matrix-Resident Proteinases. Adv Dent Res 10 (2), 159–169.

Smith, C.E.L., Poulter, J.A., Antanaviciute, A., Kirkham, J., Brookes, S.J., Inglehearn, C. F., Mighell, A.J., 2017. Amelogenesis Imperfecta; Genes, Proteins, and Pathways. Front Physiol 8, 435.

Stifler, C.A., Wittig, N.K., Sassi, M., Sun, C.-Y., Marcus, M.A., Birkedal, H., Beniash, E., Rosso, K.M., Gilbert, P.U.P.A., 2018. X-ray Linear Dichroism in Apatite. J Am Chem Soc 140 (37), 11698–11704.

Sun, C.-Y., Marcus, M.A., Frazier, M.J., Giuffre, A.J., Mass, T., Gilbert, P.U.P.A., 2017. Spherulitic growth of coral skeletons and synthetic aragonite: nature's three-dimensional printing. ACS nano 11 (7), 6612–6622.

Tadic, D., Peters, F., Epple, M., 2002. Continuous synthesis of amorphous carbonated apatites. Biomaterials 23 (12), 2553–2559.

Tao, J., Shin, Y., Jayasinha, R., Buchko, G.W., Burton, S.D., Dohnalkova, A.C., Wang, Z., Shaw, W.J., Tarasevich, B.J., 2019. The energetic basis for hydroxyapatite mineralization by amelogenin variants provides insights into the origin of *amelogenesis imperfecta*. Proc. Natl. Acad. Sci. USA 116 (28), 13867–13872.

Tao, J., Fijneman, A., Wan, J., Prajapati, S., Mukherjee, K., Fernandez-Martinez, A., Moradian-Oldak, J., De Yoreo, J.J., 2018. Control of Calcium Phosphate Nucleation and Transformation through Interactions of Enamelin and Amelogenin Exhibits the "Goldilocks Effect". Cryst Growth Des 18 (12), 7391–7400.

Wald, T., Spoutil, F., Osickova, A., Prochazkova, M., Benada, O., Kasparek, P., Bumba, L., Klein, O.D., Sedlacek, R., Sebo, P., Prochazka, J., Osicka, R., 2017. Intrinsically disordered proteins drive enamel formation via an evolutionarily conserved self-assembly motif. Proc Natl Acad Sci U S A 114 (9), E1641–E1650.

Warshawsky, H., Smith, C.E., 1971. A three-dimensional reconstruction of the rods in rat maxillary incisor enamel. Anat Rec 169 (3), 585–591.

Weatherell, J.A., Robinson, C., Hallsworth, A.S., 1974. Variations in the chemical composition of human enamel. J Dent Res 53 (2), 180–192.

Wiedemann-Bidlack, F.B., Beniash, E., Yamakoshi, Y., Simmer, J.P., Margolis, H.C., 2007. pH triggered self-assembly of native and recombinant amelogenins under physiological pH and temperature in vitro. J Struct Biol 160 (1), 57–69.

Wiedemann-Bidlack, F.B., Kwak, S.-Y., Beniash, E., Yamakoshi, Y., Simmer, J.P., Margolis, H.C., 2011. Effects of phosphorylation on the self-assembly of native full-length porcine amelogenin and its regulation of calcium phosphate formation in vitro. J Struct Biol 173 (2), 250–260.

Wilmers, J., Bargmann, S., 2020. Nature's design solutions in dental enamel: Uniting high strength and extreme damage resistance. Acta Biomater 107, 1–24.

Wright, J.T., 2006. The molecular etiologies and associated phenotypes of amelogenesis imperfecta. Am J Med Genet A 140A (23), 2547–2555.

Xu, C., Reed, R., Gorski, J.P., Wang, Y., Walker, M.P., 2012. The distribution of carbonate in enamel and its correlation with structure and mechanical properties. J. Mater. Sci. 47 (23), 8035–8043.

Yilmaz, E.D., Schneider, G.A., Swain, M.V., 2015. Influence of structural hierarchy on the fracture behaviour of tooth enamel. Philos Trans A Math Phys. Eng Sci 373 (2038), 20140130. https://doi.org/10.1098/rsta.2014.0130.

Yin, K., Paine, M.L., 2017. Bicarbonate Transport During Enamel Maturation. Calcif Tissue Int 101 (5), 457–464.